molecules

MDPI

Article

Synergistic Spatial Confining Effect and O Vacancy in WO_3 Hollow Sphere for Enhanced N_2 Reduction

Yuzhou Xia [1,2,3,†], Xinghe Xia [1,2,†], Shuying Zhu [1,*], Ruowen Liang [2], Guiyang Yan [2], Feng Chen [2,*] and Xuxu Wang [3]

[1] College of Chemistry, Fuzhou University, Fuzhou 350116, China; yzxia@ndnu.edu.cn (Y.X.); 211327039@fzu.edu.cn (X.X.)
[2] Fujian Province University Key Laboratory of Green Energy and Environment Catalysis, Ningde Normal University, Ningde 352100, China; rwliang@ndnu.edu.cn (R.L.); ygyfjnu@163.com (G.Y.)
[3] State Key Laboratory of Photocatalysis on Energy and Environment, Research Institute of Photocatalysis, College of Chemistry, Fuzhou University, Fuzhou 350116, China; xwang@fzu.edu.cn
* Correspondence: syzhu@fzu.edu.cn (S.Z.); t9309@ndnu.edu.cn (F.C.)
† These authors contributed equally to this work.

Abstract: Visible-light-driven N_2 reduction into NH_3 in pure H_2O provides an energy-saving alternative to the Haber–Bosch process for ammonia synthesizing. However, the thermodynamic stability of N≡N and low water solubility of N_2 remain the key bottlenecks. Here, we propose a solution by developing a WO_{3-x} hollow sphere with oxygen vacancies. Experimental analysis reveals that the hollow sphere structure greatly promotes the enrichment of N_2 molecules in the inner cavity and facilitates the chemisorption of N_2 onto WO_{3-x}-HS. The outer layer's thin shell facilitates the photogenerated charge transfer and the full exposure of O vacancies as active sites. O vacancies exposed on the surface accelerate the activation of N≡N triple bonds. As such, the optimized catalyst shows a NH_3 generation rate of 140.08 μmol g^{-1} h^{-1}, which is 7.94 times higher than the counterpart WO_3-bulk.

Keywords: WO_3; hollow sphere; O defect; N_2 reduction; photocatalysis

Citation: Xia, Y.; Xia, X.; Zhu, S.; Liang, R.; Yan, G.; Chen, F.; Wang, X. Synergistic Spatial Confining Effect and O Vacancy in WO_3 Hollow Sphere for Enhanced N_2 Reduction. *Molecules* **2023**, *28*, 8013. https://doi.org/10.3390/molecules28248013

Academic Editor: Chongjun Zhao

Received: 13 November 2023
Revised: 28 November 2023
Accepted: 6 December 2023
Published: 8 December 2023

1. Introduction

Ammonia synthesis becomes one of the most important industrial reactions due to the widespread use of NH_3 as fertilizers, pharmaceuticals, chemical feedstocks, and a promising clean energy carrier [1–4]. Up until now, NH_3 production has greatly relied on the Haber–Bosch nitrogen fixation process, which was awarded as one of the most significant inventions of the 20th century. However, the reductant H_2 used in this process is mainly derived from the steam reforming of biomass, and the reaction occurs under stringent reaction conditions (350–550 °C, 200–350 atm), which consumes up to ~2% of the total energy each year [5–8]. The excessive consumption of fossil energy and massive carbon dioxide emissions make this process not conducive to the sustainable development of mankind. Therefore, environmentally friendly NH_3 synthesis via a renewable route is highly desirable [9,10].

Photocatalytic N_2 reduction with H_2O assembles the advantages of low cost, safety, and environmental friendliness to produce ammonia [11,12]. The mechanism of photocatalytic N_2 reduction is as follows: N_2 is first absorbed onto the surface of the photocatalyst. Due to the strong interaction between N_2 and active sites, the sturdy triple bond is weakened, and the N_2 molecule is activated. Under irradiation, the photogenerated electrons on the conduction band of semiconductors transfer to the activated N_2 molecules, reducing N_2 into NH_3 with the participation of water. The evolved NH_3 is desorbed from the catalyst surface. Since the pioneering work reported by Schrauzer on using Fe-doped TiO_2, extensive efforts have been made to broaden the family of photocatalysts for N_2 reduction [13]. So far, diverse catalysts have been developed for photocatalytic N_2 reduction, including

BiOBr, $InVO_4$, Bi_2WO_6, $Bi_2Sn_2O_7$, and so on [14–18]. Despite much progress, the overall efficiency is still much less than satisfactory due to the bottlenecks of the extremely low solubility of N_2 in H_2O and the large dissociation energy of N≡N (941 kJ mol^{-1}) [19,20]. To tackle these, morphology and structure optimization to regulate the physical and chemical properties of photocatalysts may be effective strategies [21–25].

Hollow materials illustrate distinctive physicochemical properties due to the unique structure of the confined thin shell layer and internal cavity [26–28], presenting as ideal candidates for photocatalytic N_2 reduction. The spatial confining effect of the internal cavity is beneficial for restricting N_2, enriching N_2 molecules on the surface of the photocatalyst, thereby accelerating reaction kinetics. Moreover, the thin shell ensures the sufficient exposure of active sites. On the other hand, surface defects on photocatalysts with highly localized electronic structural changes are efficient active sites for N_2 adsorption and activation [29–32]. Especially for the O defect, the electron-rich environment is beneficial for the cleavage of the N≡N triple bond via the π-back-donation into N_2 antibonding orbitals, achieving a smoother hydrogenation process [33]. For instance, Mi and coworkers have reported the preparation of TiO_2 with O defects via a solid phase reduction with $NaBH_4$. The normalized N_2 photofixation rate is 324.86 μmol h^{-1} g^{-1}, which is 3.85 times that of the original TiO_2. The experimental and theoretical calculation results suggest that the introduced O defects play a dual role in accelerating the photocatalytic N_2 reduction efficiency. An optimized concentration of O defects as electron acceptors can increase the charge separation efficiency. On the other hand, N_2 adsorbed on OVs can be dissociated and activated through the transfer of electrons into the antibonding orbital of N_2, thus weakening the strong triple bond [34]. Thus, it is desirable to optimize N_2 reduction performance by introducing O defect active sites on hollow-structure photocatalysts.

WO_3 has been widely adopted as a promising photocatalyst due to its appropriate band gap (~2.4 eV), low conduction band edge potential, and fleet electron transport rate [35–37]. Moreover, the adjustable crystal structure makes the O defect-rich WO_3 the hotspot in N_2 reduction. For instance, Wang and coworkers have reported that the light-induced O defects at the grain boundaries of porous WO_3 can greatly enhance photocatalytic N_2 reduction performance [38]. Mechanistic studies reveal that the O defect regulates the band structure of WO_3, providing sufficient driving force to trigger N_2 reduction. Moreover, O defects can serve as active sites to chemisorb N_2 molecules. Under light, the chemisorbed N_2 molecules accepted photoexcited electrons to generate N_2H^* intermediates with coupled protons, further hydrogenating into NH_3. Chen and coworkers proposed the modification of Fe single atoms to adjust the electronic structure of O-defective WO_3 and facilitate the adsorption and conversion of N_2 [39]. These works have revealed that the introduction of the O defect is an efficient approach for promoting photocatalytic N_2 reduction in thermodynamics, but the synergistic effects of the O defect and hollow structure to further promote N_2 reduction in dynamics have not been reported.

Herein, we design a series of WO_3 hollow spheres with O defects (WO_{3-x}-HS) to accomplish efficient photocatalytic N_2 reduction into NH_3 in H_2O. The as-synthesized WO_{3-x}-HS demonstrates a superior NH_3 evolution rate of 140.1 μmol g^{-1} h^{-1}, which is 7.96 times higher than that of pristine bulk WO_3. The experimental analysis reveals that the uniform hollow sphere structure provides WO_{3-x}-HS with a relatively larger specific surface area and a confined cavity for the adsorption and enrichment of N_2 molecules on the photocatalyst, while the O defect promotes the activation of the inert N≡N triple bond.

2. Results and Discussion

The schematic synthetization of WO_{3-x}-HS is illustrated in Figure 1. Specifically, the carbon sphere has been first prepared with glucose as a precursor via a hydrothermal process. Then, W^{6+} is adsorbed onto the surface of the carbon sphere. The mixture is calcined at 450 °C to remove the template carbon sphere, and the hollow sphere structure WO_{3-x}-HS is obtained. The crystal structures of WO_{3-x}-HS and bulk WO_3 are investigated via X-ray diffraction (XRD). The diffraction peaks of both samples can be matched well

with monoclinic tungsten trioxide (PDF#20-1324) (Figure S1). The characteristic peaks at 23.1°, 23.7°, 24.1°, 28.8°, 33.3°, 33.6°, and 34.0° correspond to the (001), (020), (200), (111), (021), (201), and (220) planes of monoclinic WO_3, respectively.

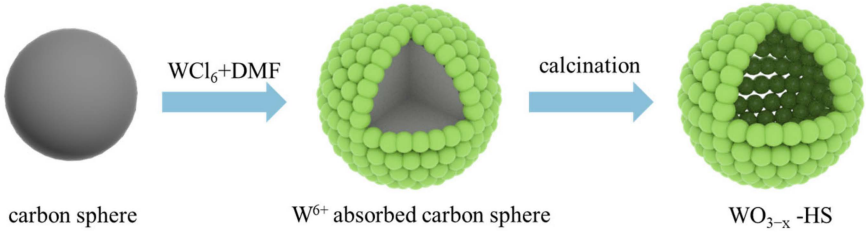

Figure 1. Schematic illustration of the synthesis of WO_{3-x}-HS.

The morphologies of the as-synthesized samples are carefully investigated via scanning electron microscopy (SEM) and transmission electron microscopy (TEM). As displayed in Figure 2a, the obtained carbon sphere exhibits a typical and uniform spherical morphology. Figure 2b–e presents the WO_{3-x}-HS samples synthesized with different amounts of template. When a 0.1 g carbon sphere is used, the obtained sample shows an amorphous structure, which may be due to the insufficient template. With the increasing amount of carbon sphere, the hollow sphere structure formed gradually. WO_{3-x}-HS synthesized with the addition of a 0.25 g template presents the most uniform and complete hollow sphere morphology. The surface is clear and smooth. As a counterpart, the WO_3-bulk exhibits an irregularly shaped block structure consisting of small particles (Figure 2f). The TEM image (Figure 2g) further reveals the sphere structure of WO_{3-x}-HS. Moreover, the brightness of the outer edge of the WO_{3-x}-HS is lower than center position, indicating that the prepared WO_{3-x}-HS is a hollow sphere with a cavity structure (Figure 2h). The high-resolution TEM (HRTEM) of WO_{3-x}-HS is shown in Figure 2i. Distinct 0.375 nm and 0.369 nm lattice fringes are observed, which correspond to the (020) and (200) crystal planes of tungsten oxide, respectively. Moreover, the elemental mapping results reveal the co-existence of W and O with uniform dispersion in WO_{3-x}-HS (Figure S2).

It is well known that the photocatalytic performance is closely related to the specific surface area size and porosity of the catalyst [40,41]. The N_2 adsorption/desorption isotherms and the pore size distribution of the obtained WO_{3-x}-HS and WO_3-bulk products are measured and presented in Figure 3a. Both catalysts have strong interactions with N_2 in the low-pressure region and show H3-type hysteresis loops in the high-pressure region, indicating that both samples have type IV adsorption–desorption isotherms [42]. The Brunauer–Emmett–Teller (BET) surface areas of WO_{3-x}-HS and WO_3-bulk are determined to be 23.71 $m^2\ g^{-1}$ and 8.53 $m^2\ g^{-1}$, respectively. The larger surface areas of WO_{3-x}-HS are expected to expose more catalytically active sites and enhance the contact and adsorption of nitrogen molecules. The pore size distribution curves confirm the presence of mesopores (2–50 nm) in both samples, and the porosities of WO_{3-x}-HS and WO_3-bulk are 0.077 $cm^3\ g^{-1}$ and 0.043 $cm^3\ g^{-1}$, respectively. The larger porosity of WO_{3-x}-HS can accelerate the transport of reactants and products during N_2 photocatalytic nitrogen fixation, providing more opportunities for proton capture and the deep hydrogenation of intermediates in photocatalytic nitrogen fixation. The presence of oxygen vacancy is verified using electron paramagnetic resonance (EPR). As can be seen in Figure 3b, no signal is observed for WO_3-bulk in the whole range. While a significant resonance peak at g-factor value of 2.003 ascribed to the unpaired electrons is observed, suggesting the existence of abundant O vacancies in WO_{3-x}-HS [23]. The possible O vacancy formation mechanism may be that the removal of the reductive carbon template induces the escape of lattice oxygen. The optical properties of the obtained photocatalysts have been evaluated using diffuse reflectance spectroscopy (DRS). As shown in Figure 3c, the absorption edge of WO_{3-x}-HS shows a blue-shift when compared with WO_3-bulk. Moreover, WO_{3-x}-HS exhibits stronger light absorption properties in the visible light region, which may be due to the existence of a "sub-band" induced by O vacancies. The band energies (E_g value) of the catalysts

are calculated using Tauc fitting curves (Figure 3d) [43]. The E_g values of WO_{3-x}-HS and WO_3-bulk are determined to be 2.30 and 2.43 eV, respectively.

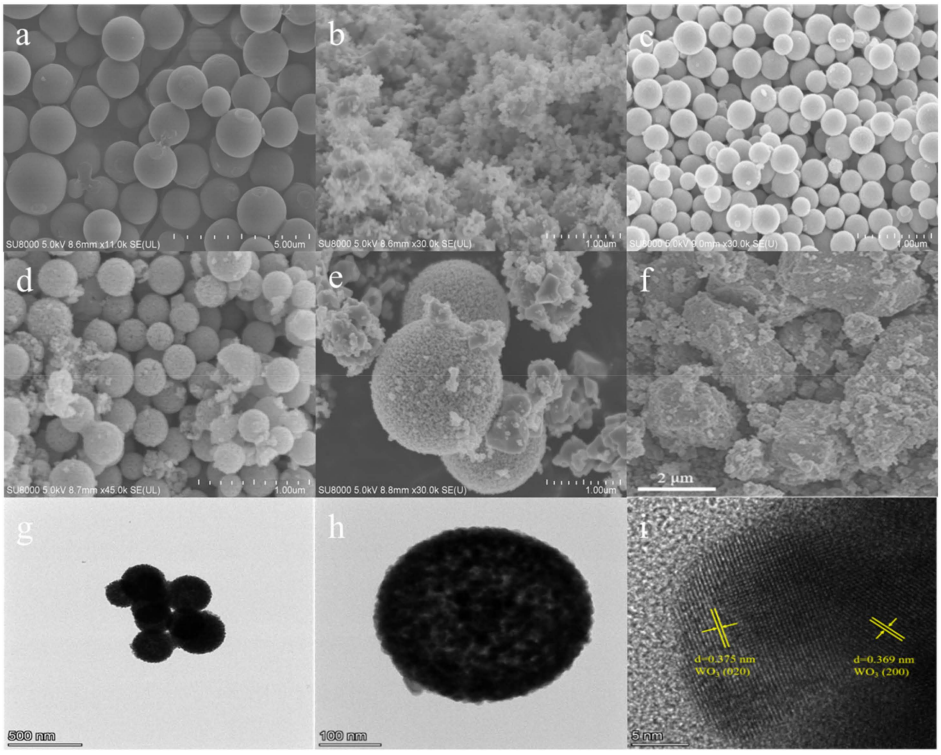

Figure 2. SEM images of carbon sphere (**a**). WO_{3-x}-HS samples synthesized with various amounts of carbon sphere template: 0.1 g (**b**), 0.25 g (**c**), 0.4 g (**d**), 0.5 g (**e**), and WO_3-bulk (**f**). TEM (**g**,**h**) and HRTEM images (**i**) of WO_{3-x}-HS.

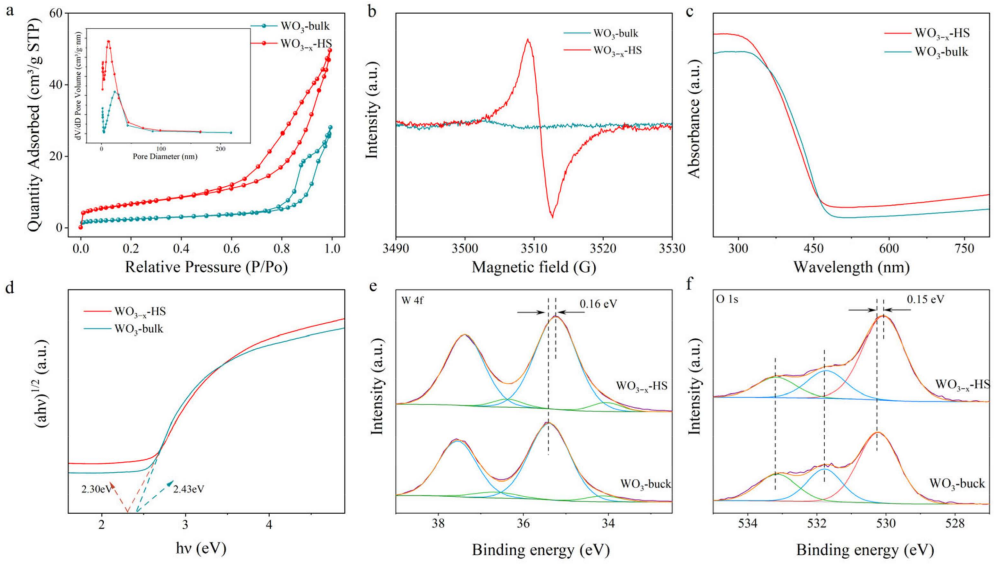

Figure 3. BET (**a**), EPR (**b**), DRS (**c**), Tauc plots (**d**), high-resolution XPS spectra of W 4f (**e**) and O 1s (**f**) of WO_{3-x}-HS and WO_3-bulk.

The surface chemical state of elements of as-synthesized samples has been evaluated using an X-ray photoelectron spectroscope (XPS) (Figure 3e,f). The W 4f spectra of both samples are deconvoluted into two doublet peaks, associated with two different states of the W element. The peaks in WO_3-bulk at the binding energies at 35.39 and 37.55 eV correspond to the W $4f_{7/2}$ and W $4f_{5/2}$ signals of W^{6+}. The second doublet peaks at

34.12 and 36.67 eV are assigned to the W $4f_{7/2}$ and W $4f_{5/2}$ of W^{5+}. Note that the W 4f binding energies of WO_{3-x}-HS are lower than those of WO_3-bulk, indicating a decrease in electron density after the generation of O vacancies [44]. The O 1s spectrum of WO_3-bulk can be fitted with three peaks at the binding energies of 530.22, 531.78, and 533.15 eV, which are attributed to the lattice oxygen, O in the surface hydroxyl group, and chemisorbed oxygen, respectively [45]. There is a decrease in the binding energy of lattice oxygen in WO_{3-x}-HS when compared to that of WO_3-bulk, which is attributable to the increased electron cloud density caused by the formation of O vacancies.

The photocatalytic nitrogen reduction reaction (NRR) activities of the as-synthesized samples have been evaluated with H_2O and N_2 as feedstocks. Figure 4a shows the performance of WO_{3-x}-HS prepared with different amounts of carbon sphere as a template. It is interesting to see that the NH_3 generation rates exhibit a trend of increasing initially and decreasing afterwards with the increasing amount of carbon sphere. The WO_{3-x}-HS synthesized with the addition of a 0.25 g template presents the optimal NRR activity, with an ammonia production rate of 140.08 μmol g^{-1} h^{-1}. It can also be seen that the prepared WO_{3-x}-HS exhibits better performance than most of the reported works on photocatalytic N_2 reduction (Table S1). It seems to match with the SEM results that a higher NRR performance is achieved with a more complete hollow sphere structure. The high performance of NRR over WO_{3-x} is also confirmed by ion chromatography (Figure 4b). To further reveal the role of hollow structure and O vacancies in effecting the photocatalytic performance, the NRR activity of WO_3-bulk is tested. As displayed in Figure 4c, the WO_3-bulk exhibits a relatively low NH_3 generation rate of 17.64 μmol g^{-1} h^{-1}. The possible reasons may be that the hollow sphere structure of WO_{3-x}-HS with a larger specific surface area exposes more active sites of O vacancies to activate the N≡N. The hollow structure with a nanoconfined cavity promotes the reaction kinetics. The photocatalytic performance of WO_{3-x}-HS under different reaction conditions has been investigated. As can be seen from Figure 4d, when the gas is changed from N_2 to Ar, almost no ammonia is produced. At the same time, ammonia could not be detected without a catalyst or in dark conditions. All these results elucidate that the evolved NH_3 is indeed originated from N_2 through the photocatalytic reduction process.

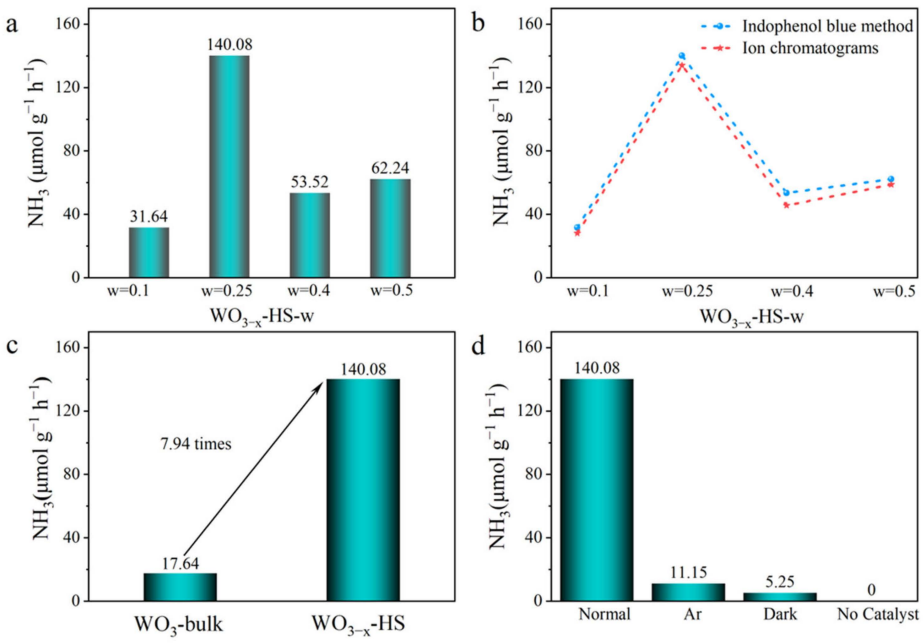

Figure 4. Photocatalytic N_2 reduction performance of WO_{3-x}-HS-w prepared with different amounts of carbon sphere as template (**a**); comparison of two methods for determining ammonia concentration (**b**); comparison of photocatalytic N_2 reduction performance of WO_{3-x}-HS and WO_3-bulk (**c**); control experiments of WO_{3-x}-HS for photocatalytic N_2 reduction performance under different conditions (**d**).

The WO_{3-x}-HS synthesized with the addition of 0.25 g of template showed the best NRR activity with an ammonia generation rate of 140.08 μmol g^{-1} h^{-1}. The prepared WO_{3-x}-HS outperforms most of the reported research results in photocatalytic reduction of N_2 (Table S1). This seems to be in agreement with the SEM results that a more complete hollow sphere structure can achieve higher NRR performance.

Linear scanning voltammetry (LSV) tests have been performed on WO_{3-x}-HS and WO_3-bulk in Ar- and N_2-saturated electrolyte environments to evaluate the NRR performance. A distinct current density enhancement under N_2 over Ar suggests a potential NRR process driven by both samples (Figure 5a). The photocurrent densities of WO_{3-x}-HS in a N_2 environment are much higher than those of WO_3-bulk, indicating better NRR activity [46]. Electrochemical characterizations have been performed to reveal the charge transfer and separation behaviors. Figure 5b shows the transient photocurrent response of the sample. The photocurrent density of WO_{3-x}-HS is significantly higher compared to WO_3-bulk, indicating that the WO_{3-x}-HS material is more capable of photo-induced electron–hole pair separation [47]. Electrochemical impedance spectroscopy (EIS) is used to monitor charge transfer behavior. As shown in Figure 5c, WO_{3-x}-HS presents a decreased semicircle compared to the WO_3-bulk, indicating lower electron transfer resistance [48]. These results demonstrate that the O vacancies on WO_{3-x}-HS contribute to the improved separation and transfer of photoinduced carriers. The evaluation of carrier separation efficiency is conducted via steady-state PL emission spectroscopy. As shown in Figure 5d, under excitation light at a wavelength of 453 nm, there is an obvious PL quenching of WO_{3-x}-HS compared to WO_3-bulk, indicating the photogenerated electron–hole recombination is suppressed and the photogenerated carrier utilization efficiency is higher [49]. The reason for this result may be that the hollow structure with a relatively thin shell of WO_{3-x}-HS is beneficial for the migration rate and separation efficiency of photogenerated carriers.

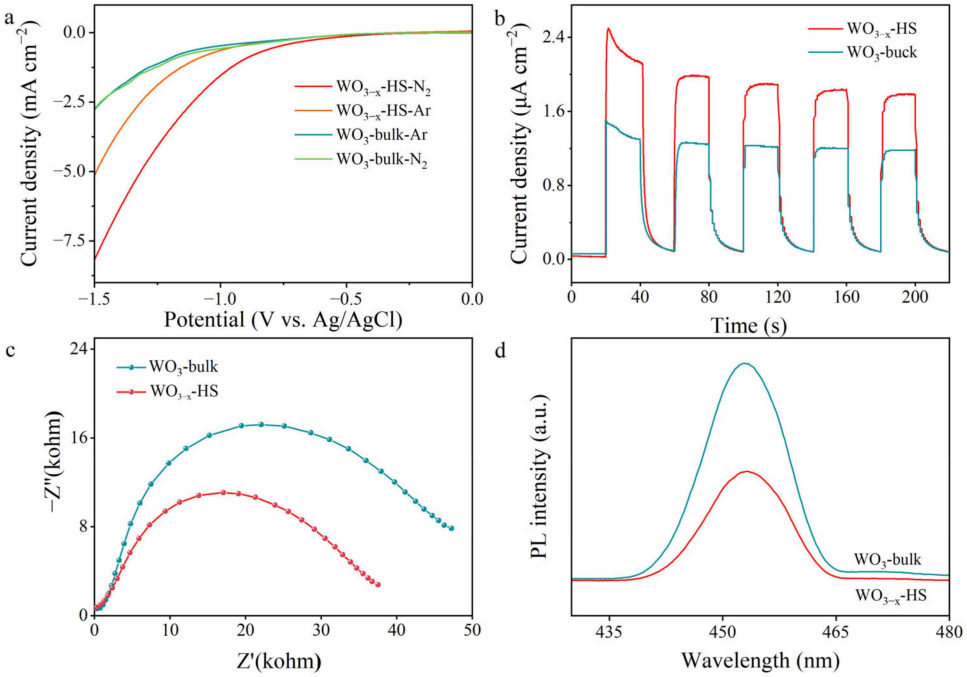

Figure 5. LSV curves (**a**), transient photocurrent responses (**b**), EIS Nyquist plots (**c**), and PL spectra (**d**) of WO_{3-x}-HS and WO_3-bulk.

The N_2 adsorption performance of the catalysts was characterized using N_2 temperature-programmed desorption spectrometry (N_2-TPD). As shown in Figure 6a, both WO_{3-x}-HS and WO_3-bulk show adsorption peaks at low (230–360 °C) and high temperatures (470–650 °C), which are attributed to the physical adsorption and chemical adsorption peaks of N_2, respectively [50]. The peak intensities of WO_{3-x}-HS are stronger than those of WO_3-bulk, and the

peak position shows a positive shift to the relatively high temperature, which certifies the much-improved N_2 affinity. These results reveal that the designed hollow sphere structure with confined inner micro-space and O vacancies are beneficial for the adsorption of N_2 molecules and for facilitating the NRR process.

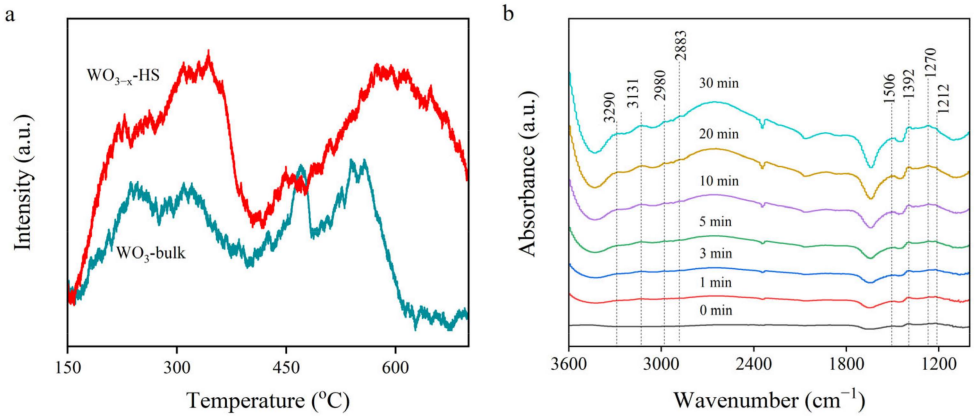

Figure 6. N_2-TPD of WO_{3-x}-HS and WO_3-bulk (**a**); in situ DRIFTS spectra of WO_{3-x}-HS during photocatalytic N_2 fixation process (**b**).

In situ diffuse reflectance infrared Fourier transform spectroscopy (in situ DRIFTS) has been tested to reveal the possible N_2 reduction process. The WO_{3-x}-HS catalyst is exposed to a vapor of N_2 and water to simulate the reaction conditions. The in situ DRIFTS is recorded with different light irradiation times. As shown in Figure 6b, the peak at 1506 cm^{-1} can be attributed to the OH bending mode of adsorbed water [51]. When light is introduced, the newly emerged peak at 3290 cm^{-1} is attributed to the ν(N-H) stretching mode in the reacting intermediate [52]. The signals at about 1212, 1270, and 1392 cm^{-1} are assigned to bending vibrations of ammonia species and intermediates σ(N-H), while the peaks at about 2883 and 2980 cm^{-1} are absorption peaks of NH_4^+ [51,53]. Moreover, these peaks intensified with prolonged irradiation time, revealing that N_2 is gradually hydrogenated to ammonia over the catalyst consistently.

Mott–Schottky tests were performed to evaluate the energy band positions of WO_{3-x}-HS (Figure 7a). The slope of the linear potential curves of WO_{3-x}-HS is positive, indicating that the as-synthesized sample is an n-type semiconductor material [54]. The flat band potentials of WO_{3-x}-HS are determined to be −0.33 V (vs. Ag/AgCl, pH = 7), corresponding to −0.133 V vs. NHE based on the equation ($E_{NHE} = E_{Ag/AgCl} + 0.197$) [55]. The conduction band of n-type semiconductors is 0–0.1 V higher than the flat-band potential. Here, the voltage difference between the conduction band (CB) and the flat potential is set to 0 V; thus, the minimum conduction band (CB) for WO_{3-x}-HS is about −0.13 V (vs. NHE, pH = 7). Combined with the DRS result, the valence bands (VB) of WO_{3-x}-HS are calculated to be 2.17 V (vs. NHE, pH = 7) [56]. Thus, the band structure of WO_{3-x}-HS is shown in Figure 7b. Apparently, it is thermodynamically favorable for the CB electrons to reduce N_2 into NH_3 and VB holes to oxidize H_2O.

A possible NRR mechanism for WO_{3-x}-HS has been proposed. In the reaction system, N_2 molecules are confined and enriched in the inner cavity of WO_{3-x}-HS. Beneficiating from the thin shell of the hollow structure, O vacancies in WO_{3-x}-HS are sufficiently exposed as active sites. Thus, the activation of the N≡N triple bond is achieved by the electron-rich environment of O vacancies via the π-back-donation into N_2 antibonding orbitals. Upon irradiation, photogenerated holes on the VB of WO_{3-x}-HS oxidize H_2O into O_2 and release active protons. The electrons accumulated on the CB reduce the activate $^*N_2$ into NH_3.

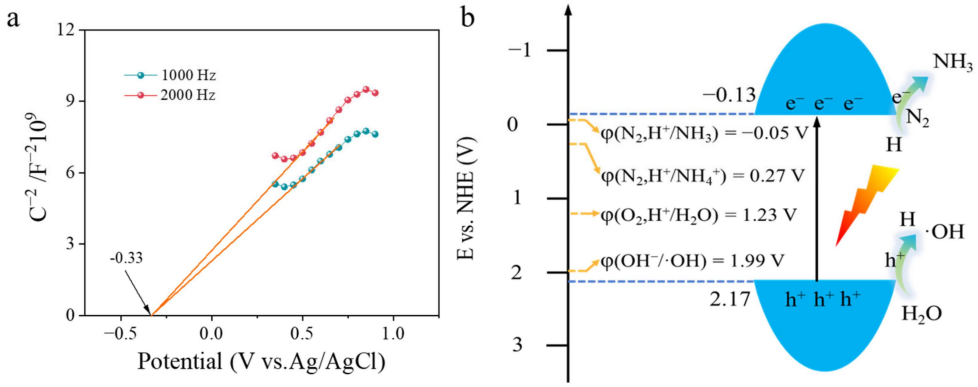

Figure 7. Mott–Schottky plots of WO_{3-x}-HS (**a**) and a schematic illustration of the band structure of WO_{3-x}-HS (**b**).

3. Materials and Methods

3.1. Materials and Reagents

Tungsten chloride (WCl_6) was purchased from Aladdin. Glucose ($C_6H_{12}O_6{\cdot}H_2O$), cetyltrimethylammonium bromide ($C_{19}H_{42}BrN$), sodium tungstate dihydrate ($Na_2WO_4{\cdot}2H_2O$), N, N-dimethylformamide (C_3H_7NO), and ethanol (C_2H_6O) were from Sinopharm Chemical Reagent Co., Ltd. (Shanghai, China). Nitric acid (HNO_3) was purchased from Xilong Science Co. (Shantou, Shantou, China). Deionized water (18.2 MΩ cm) was obtained from a waterproof system and used in all experiments. All chemicals used in this work were of analytical grade. None of the above reagents required further purification.

3.2. The Preparation of Carbon Nanosphere

Carbon nanospheres were prepared by glucose under hydrothermal conditions. An amount of 6 g of glucose was dissolved in 6 mL of deionized water. The solution was transferred to a 100 mL of PTFE reactor and reacted at 180 °C for 12 h in an oven. After the hydrothermal reaction was completed, the supernatant was centrifugally washed with deionized water and ethanol until the ionic solubility of the supernatant was less than 10 ppm. The final product was dried in a vacuum oven at 40 °C for 12 h.

3.3. The Preparation of WO_{3-x}-HS

WO_{3-x}-HS was prepared by controlling the gradual hydrolysis of WCl_6 on the template carbon sphere particles. WCl_6 was used as the metal precursor and dissolved into N, N-dimethylformamide (DMF) with a concentration of 0.1 g mL^{-1} denoted as solution A. At the same time, various amounts of carbon nanospheres (0.1, 0.25, 0.4, and 0.5 g) and 0.1 g of cetyltrimethylammonium bromide (CTAB) were dispersed into 50 mL of DMF solution and denoted as solution B. Afterwards, solution A was dropped into solution B under continuous ultrasonic treatment for 30 min. After that, 1 mL of deionized water was added dropwise to make the WCl_6 hydrolyze. The suspension was stirred at room temperature for 24 h, then washed with anhydrous ethanol and water, and finally freeze-dried. The obtained product was calcined in a muffle furnace at 450 °C for 2 h and marked as WO_{3-x}-HS.

3.4. The Preparation of Bulk WO_3

Firstly, 4 g of $Na_2WO_4{\cdot}2H_2O$ was dissolved in 20 mL water to obtain a homogeneous solution, then 50 mL HNO_3 solution (1 mol L^{-1}) was dropped into the above solution and stirred for another hour. The precipitate was washed with deionized water and ethanol and dried in a vacuum oven at 60 °C. Finally, the dried sample was grounded and calcined at 450 °C for 2 h, denoted as WO_3-bulk.

3.5. Photocatalytic N_2 Fixation

The photocatalytic nitrogen fixation reaction was carried out at room temperature by first adding the photocatalyst (0.015 g) and 50 mL of deionized water to a quartz reactor with a quartz top and sonicating for 3 min. The reactor was then evacuated and subsequently bubbled with ultrapure N_2 for 30 min in the darkness. Finally, the reaction was carried out under the illumination of a 300 W xenon lamp (CEL-HXF300-T3 with filter (420 nm < λ < 800 nm)) for 1 h with continuously bubbling N_2 in the whole reaction process. A quantity of the reaction solution was collected, filtered, and then assayed for ammonia concentration by the indophenol blue method. The average ammonia concentration was calculated by three parallel experiments. The calibration curve of NH^{4+} measured by UV-vis spectra is displayed in Figure S3.

3.6. Characterization

The crystal structure of the photocatalysts was analyzed by X-ray electron diffraction on a Bruker D8 Advance X-ray diffractometer. The morphological and lattice structure information was characterized using scanning electron microscopy (Hitachi SU8000, Tokyo, Japan) and transmission electron microscopy (FEI Talos F200s, Hillsboro, OR, USA). Ultraviolet-visible diffuse reflectance spectroscopy was measured on a Varian Cary 500 UV-vis spectrophotometer. The chemical states of the prepared samples were characterized via X-ray photoelectron spectroscopy on a VG Scientific ESCA Lab Mark II spectrometer. The binding energies of all tested elements were calibrated by C 1s at 284.6 eV. Electron paramagnetic resonance measurements were performed on a Bruker A300 EPR spectrometer. Electrochemical tests were performed on a ZENNIUM IM6 electrochemical workstation (Zahner, Kronach, Bayern, Germany). The chemisorption properties of the catalyst for N_2 were characterized using N_2 temperature-programmed desorption spectrometry on an AutoChem II 2920 (Micromeritics) instrument with a thermal conductivity detector. PL was measured by a fluorophotometer (Edinburgh FLS1000) with an excitation wave length of 453 nm.

3.7. Electrochemistry Measurement

Fluorine-doped tin oxide (FTO) glass was used for the preparation of the working electrode. The FTO glass was first washed by sonication in acetone and ethanol for 30 min. Next, 5 mg of the as-synthesized samples were added to 0.5 mL N, N-dimethylformamide. The mixture was continuously sonicated for 2 h to obtain a uniform slurry. Then, 10 μL of the obtained homogeneous slurry was dropped onto the FTO side with exposed areas of 0.25 cm^2. The remaining parts that were not coated were sealed with epoxy resin. Finally, the electrode was dried in nature. A conventional three-electrode cell was used for the electrochemical tests. A Pt plat and a Ag/AgCl electrode were adopted as counter electrodes and reference electrodes, respectively. Na_2SO_4 aqueous was used as an electrolyte.

4. Conclusions

In summary, we have developed a WO_{3-x} hollow sphere with oxygen defects for efficient N_2 photoreduction into NH_3. It is revealed that the hollow sphere structure greatly promotes the enrichment of N_2 molecules in the inner cavity and facilitates the chemisorption of N_2 onto WO_{3-x}-HS. O vacancies exposed on the surface accelerate the activation of the N≡N triple bond. Moreover, the thin shell of the hollow structure facilitates the photogenerated charge transfer. As such, the WO_{3-x}-HS exhibits better photocatalytic NRR activity with an optimal NH_3 generation rate of 140.08 μmol g^{-1} h^{-1}, which is 7.94 times higher than the counterpart WO_3-bulk. This work validates an avenue for designing active photocatalysts toward N_2 reduction via morphology and structure regulation.

Supplementary Materials: The following supporting information can be downloaded at: https://www.mdpi.com/article/10.3390/molecules28248013/s1, Figure S1: XRD pattern of WO_{3-x}-HS and WO_3-bulk; Figure S2: HAADF-STEM (a) and corresponding elemental mapping images W (b) and O (c) of WO_{3-x}-HS; Figure S3: The calibration curve of NH_4^+ reference by UV-vis spectra at room temperature; Table S1: Comparison of photocatalytic N_2 reduction performance among reported catalysts. References [57–67] are citation in the Supplementary Materials.

Author Contributions: Conceptualization, Y.X. and X.X.; methodology, Y.X.; validation, X.X. and Y.X.; formal analysis, Y.X. and X.X.; investigation, Y.X. and X.X.; resources, X.W.; data curation, X.X. and Y.X.; writing—original draft preparation, X.X.; writing—review and editing, Y.X., S.Z. and R.L.; supervision, X.W. and F.C.; project administration, G.Y.; funding acquisition, F.C. and Y.X. All authors have read and agreed to the published version of the manuscript.

Funding: This work was supported by the National Natural Science Foundation of China (22108129, 22372085); and Natural Science Foundation of Ningde Normal University (2022T02).

Institutional Review Board Statement: Not applicable.

Informed Consent Statement: Not applicable.

Data Availability Statement: Data are contained within the article and Supplementary Materials.

Conflicts of Interest: The authors declare no conflict of interest.

References

1. Canfield, D.E.; Glazer, A.N.; Falkowski, P.G. The Evolution and Future of Earth's Nitrogen Cycle. *Science* **2010**, *330*, 192–196. [CrossRef] [PubMed]
2. Li, P.; Zhou, Z.; Wang, Q.; Guo, M.; Chen, S.; Low, J.; Long, R.; Liu, W.; Ding, P.; Wu, Y.; et al. Visible-Light-Driven Nitrogen Fixation Catalyzed by Bi_5O_7Br Nanostructures: Enhanced Performance by Oxygen Vacancies. *J. Am. Chem. Soc.* **2020**, *142*, 12430–12439. [CrossRef] [PubMed]
3. Chen, J.G.; Crooks, R.M.; Seefeldt, L.C.; Bren, K.L.; Bullock, R.M.; Darensbourg, M.Y.; Holland, P.L.; Hoffman, B.; Janik, M.J.; Jones, A.K.; et al. Beyond Fossil Fuel-Driven Nitrogen Transformations. *Science* **2018**, *360*, eaar6611. [CrossRef] [PubMed]
4. Erisman, J.W.; Sutton, M.A.; Galloway, J.; Klimont, Z.; Winiwarter, W. How a Century of Ammonia Synthesis Changed the World. *Nat. Geosci.* **2008**, *1*, 636–639. [CrossRef]
5. Gao, X.; Shang, Y.; Liu, L.; Fu, F. Chemisorption-Enhanced Photocatalytic Nitrogen Fixation via 2D Ultrathin p-n Heterojunction AgCl/δ-Bi_2O_3 Nanosheets. *J. Catal.* **2019**, *371*, 71–80. [CrossRef]
6. Schlögl, R. Catalytic Synthesis of Ammonia-A "Never-Ending Story"? *Angew. Chem. Int. Ed.* **2003**, *42*, 2004–2008. [CrossRef]
7. Hoffman, B.M.; Lukoyanov, D.; Yang, Z.-Y.; Dean, D.R.; Seefeldt, L.C. Mechanism of Nitrogen Fixation by Nitrogenase: The Next Stage. *Chem. Rev.* **2014**, *114*, 4041–4062. [CrossRef] [PubMed]
8. Liu, H.; Wu, P.; Li, H.; Chen, Z.; Wang, L.; Zeng, X.; Zhu, Y.; Jiang, Y.; Liao, X.; Haynes, B.S.; et al. Unravelling the Effects of Layered Supports on Ru Nanoparticles for Enhancing N_2 Reduction in Photocatalytic Ammonia Synthesis. *Appl. Catal. B* **2019**, *259*, 118026. [CrossRef]
9. Wang, S.; Ichihara, F.; Pang, H.; Chen, H.; Ye, J. Nitrogen Fixation Reaction Derived from Nanostructured Catalytic Materials. *Adv. Funct. Mater.* **2018**, *28*, 1803309. [CrossRef]
10. Zhu, S.; Liang, S.; Bi, J.; Liu, M.; Zhou, L.; Wu, L.; Wang, X. Photocatalytic Reduction of CO_2 with H_2O to CH_4 over Ultrathin $SnNb_2O_6$ 2D Nanosheets under Visible Light Irradiation. *Green Chem.* **2016**, *18*, 1355–1363. [CrossRef]
11. Luo, J.; Bai, X.; Li, Q.; Yu, X.; Li, C.; Wang, Z.; Wu, W.; Liang, Y.; Zhao, Z.; Liu, H. Band Structure Engineering of Bioinspired Fe Doped $SrMoO_4$ for Enhanced Photocatalytic Nitrogen Reduction Performance. *Nano Energy* **2019**, *66*, 104187. [CrossRef]
12. Qiu, P.; Xu, C.; Zhou, N.; Chen, H.; Jiang, F. Metal-Free Black Phosphorus Nanosheets-Decorated Graphitic Carbon Nitride Nanosheets with C-P Bonds for Excellent Photocatalytic Nitrogen Fixation. *Appl. Catal. B* **2018**, *221*, 27–35. [CrossRef]
13. Schrauzer, G.N.; Guth, T.D. Photolysis of Water and Photoreduction of Nitrogen on Titanium Dioxide. *J. Am. Chem. Soc.* **1977**, *99*, 7189–7193. [CrossRef]
14. Liu, J.; Li, R.; Zu, X.; Zhang, X.; Wang, Y.; Wang, Y.; Fan, C. Photocatalytic Conversion of Nitrogen to Ammonia with Water on Triphase Interfaces of Hydrophilic-Hydrophobic Composite $Bi_4O_5Br_2$/ZIF-8. *Chem. Eng. J.* **2019**, *371*, 796–803. [CrossRef]
15. Cao, S.-W.; Yin, Z.; Barber, J.; Boey, F.Y.C.; Loo, S.C.J.; Xue, C. Preparation of Au-$BiVO_4$ Heterogeneous Nanostructures as Highly Efficient Visible-Light Photocatalysts. *ACS Appl. Mater. Interfaces* **2011**, *4*, 418–423. [CrossRef] [PubMed]
16. Han, Q.; Bai, X.; Chen, J.; Feng, S.; Gao, W.; Tu, W.; Wang, X.; Wang, J.; Jia, B.; Shen, Q.; et al. Hollow $InVO_4$ Nanocuboid Assemblies toward Promoting Photocatalytic N_2 Conversion Performance. *Adv. Mater.* **2021**, *33*, 2006780. [CrossRef] [PubMed]
17. Fei, T.; Yu, L.; Liu, Z.; Song, Y.; Xu, F.; Mo, Z.; Liu, C.; Deng, J.; Ji, H.; Cheng, M.; et al. Graphene Quantum Dots Modified Flower like Bi_2WO_6 for Enhanced Photocatalytic Nitrogen Fixation. *J. Colloid Interface Sci.* **2019**, *557*, 498–505. [CrossRef] [PubMed]

18. Zhang, Y.; Di, J.; Qian, X.; Ji, M.; Tian, Z.; Ye, L.; Zhao, J.; Yin, S.; Li, H.; Xia, J. Oxygen Vacancies in $Bi_2Sn_2O_7$ Quantum Dots to Trigger Efficient Photocatalytic Nitrogen Reduction. *Appl. Catal. B* **2021**, *299*, 120680. [CrossRef]
19. Wang, L.; Xia, Y.; Yu, J. Hydrogen-Bond Activation of N_2 Molecules and Photocatalytic Nitrogen Fixation. *Chem* **2021**, *7*, 1983–1985. [CrossRef]
20. Chen, S.; Liu, D.; Peng, T. Fundamentals and Recent Progress of Photocatalytic Nitrogen-Fixation Reaction over Semiconductors. *Sol. RRL* **2020**, *5*, 2000487. [CrossRef]
21. Wang, L.; Zhang, Q.; Wei, T.; Li, F.; Sun, Z.; Xu, L. WC and Cobalt Nanoparticles Embedded in Nitrogen-Doped Carbon 3D Nanocage Derived from $H_3PW_{12}O_{40}$@ZIF-67 for Photocatalytic Nitrogen Fixation. *J. Mater. Chem. A* **2021**, *9*, 2912–2918. [CrossRef]
22. Gao, K.; Zhang, C.; Zhang, Y.; Zhou, X.; Gu, S.; Zhang, K.; Wang, X.; Song, X. Oxygen Vacancy Engineering of Novel Ultrathin $Bi_{12}O_{17}Br_2$ Nanosheets for Boosting Photocatalytic N_2 Reduction. *J. Colloid Interface Sci.* **2022**, *614*, 12–23. [CrossRef] [PubMed]
23. Wang, T.; Feng, C.; Liu, J.; Wang, D.; Hu, H.; Hu, J.; Chen, Z.; Xue, G. Bi_2WO_6 Hollow Microspheres with High Specific Surface Area and Oxygen Vacancies for Efficient Photocatalysis N_2 Fixation. *Chem. Eng. J.* **2021**, *414*, 128827. [CrossRef]
24. Cai, J.; Peng, Y.; Jiang, Y.; Li, L.; Wang, H.; Li, K. Photodegradation and Removal of Air and Water Pollutants: A Review. *Molecules* **2023**, *28*, 7121. [CrossRef] [PubMed]
25. Liao, Y.; Qian, J.; Xie, G.; Han, Q.; Dang, W.; Wang, Y.; Lv, L.; Zhao, S.; Luo, L.; Zhang, W.; et al. 2D-Layered Ti_3C_2 MXenes for Promoted Synthesis of NH_3 on P25 Photocatalysts. *Appl. Catal. B* **2020**, *273*, 119054. [CrossRef]
26. Liccardo, L.; Bordin, M.; Sheverdyaeva, P.M.; Belli, M.; Moras, P.; Vomiero, A.; Moretti, E. Surface Defect Engineering in Colored TiO_2 Hollow Spheres Toward Efficient Photocatalysis. *Adv. Funct. Mater.* **2023**, *33*, 2212486. [CrossRef]
27. Hu, W.; Zhou, W.; Zhang, K.; Zhang, X.; Wang, L.; Jiang, B.; Tian, G.; Zhao, D.; Fu, H. Facile Strategy for Controllable Synthesis of Stable Mesoporous Black TiO_2 Hollow Spheres with Efficient Solar-Driven Photocatalytic Hydrogen Evolution. *J. Mater. Chem. A* **2016**, *4*, 7495–7502. [CrossRef]
28. Wang, Y.; Huang, H.; Zhang, Z.; Wang, C.; Yang, Y.; Li, Q.; Xu, D. Lead-Free Perovskite $Cs_2AgBiBr_6$@g-C_3N_4 Z-Scheme System for Improving CH_4 Production in Photocatalytic CO_2 Reduction. *Appl. Catal. B* **2021**, *282*, 119570. [CrossRef]
29. Zanardo, D.; Forghieri, G.; Ghedini, E.; Menegazzo, F.; Giordana, A.; Cerrato, G.; Cattaruzza, E.; Di Michele, A.; Cruciani, G.; Signoretto, M. Effect of the Synthetic Parameters over ZnO in the CO_2 Photoreduction. *Molecules* **2023**, *28*, 4798. [CrossRef]
30. Liu, S.; Wang, Y.; Wang, S.; You, M.; Hong, S.; Wu, T.-S.; Soo, Y.-L.; Zhao, Z.; Jiang, G.; Qiu, J.; et al. Photocatalytic Fixation of Nitrogen to Ammonia by Single Ru Atom Decorated TiO_2 Nanosheets. *ACS Sustain. Chem. Eng.* **2019**, *7*, 6813–6820. [CrossRef]
31. Zhang, N.; Jalil, A.; Wu, D.; Chen, S.; Liu, Y.; Gao, C.; Ye, W.; Qi, Z.; Ju, H.; Wang, C.; et al. Refining Defect States in $W_{18}O_{49}$ by Mo Doping: A Strategy for Tuning N_2 Activation towards Solar-Driven Nitrogen Fixation. *J. Am. Chem. Soc.* **2018**, *140*, 9434–9443. [CrossRef] [PubMed]
32. Li, H.; Shang, J.; Ai, Z.; Zhang, L. Efficient Visible Light Nitrogen Fixation with BiOBr Nanosheets of Oxygen Vacancies on the Exposed {001} Facets. *J. Am. Chem. Soc.* **2015**, *137*, 6393–6399. [CrossRef] [PubMed]
33. Du, Y.; Jiang, C.; Song, L.; Gao, B.; Gong, H.; Xia, W.; Sheng, L.; Wang, T.; He, J. Regulating Surface State of WO_3 Nanosheets by Gamma Irradiation for Suppressing Hydrogen Evolution Reaction in Electrochemical N_2 Fixation. *Nano Res.* **2020**, *13*, 2784–2790. [CrossRef]
34. Zhang, G.; Yang, X.; He, C.; Zhang, P.; Mi, H. Constructing a Tunable Defect Structure in TiO_2 for Photocatalytic Nitrogen Fixation. *J. Mater. Chem. A* **2020**, *8*, 334–341. [CrossRef]
35. Mi, Q.; Ping, Y.; Li, Y.; Cao, B.; Brunschwig, B.S.; Khalifah, P.G.; Galli, G.A.; Gray, H.B.; Lewis, N.S. Thermally Stable N_2-Intercalated WO_3 Photoanodes for Water Oxidation. *J. Am. Chem. Soc.* **2012**, *134*, 18318–18324. [CrossRef] [PubMed]
36. Lu, C.; Cao, D.; Zhang, H.; Gao, L.; Shi, W.; Guo, F.; Zhou, Y.; Liu, J. Boosted Tetracycline and Cr(VI) Simultaneous Cleanup over Z-Scheme WO_3/CoO p-n Heterojunction with 0D/3D Structure under Visible Light. *Molecules* **2023**, *28*, 4727. [CrossRef] [PubMed]
37. Li, W.J.; Da, P.M.; Zhang, Y.Y.; Wang, Y.C.; Lin, X.; Gong, X.G.; Zheng, G.F. WO_3 Nanoflakes for Enhanced Photoelectrochemical Conversion. *ACS Nano* **2014**, *8*, 11770–11777. [CrossRef]
38. Hou, T.; Xiao, Y.; Cui, P.; Huang, Y.; Tan, X.; Zheng, X.; Zou, Y.; Liu, C.; Zhu, W.; Liang, S.; et al. Operando Oxygen Vacancies for Enhanced Activity and Stability toward Nitrogen Photofixation. *Adv. Energy Mater.* **2019**, *9*, 1902319. [CrossRef]
39. Hu, B.; Wang, B.-H.; Chen, L.; Bai, Z.-J.; Zhou, W.; Guo, J.-K.; Shen, S.; Xie, T.-L.; Au, C.-T.; Jiang, L.-L.; et al. Electronic Modulation of the Interaction between Fe Single Atoms and $WO_{2.72-x}$ for Photocatalytic N_2 Reduction. *ACS Catal.* **2022**, *12*, 11860–11869. [CrossRef]
40. Zhang, Y.; Ran, L.; Zhang, Y.; Zhai, P.; Wu, Y.; Gao, J.; Li, Z.; Zhang, B.; Wang, C.; Fan, Z.; et al. Two-Dimensional Defective Boron-Doped Niobic Acid Nanosheets for Robust Nitrogen Photofixation. *ACS Nano* **2021**, *15*, 17820–17830. [CrossRef]
41. Xia, Y.; Li, Q.; Lv, K.; Li, M. Heterojunction Construction between TiO_2 Hollowsphere and $ZnIn_2S_4$ Flower for Photocatalysis Application. *Appl. Surf. Sci.* **2017**, *398*, 81–88. [CrossRef]
42. Liang, M.; Borjigin, T.; Zhang, Y.; Liu, B.; Liu, H.; Guo, H. Controlled Assemble of Hollow Heterostructured g-C_3N_4@CeO_2 with Rich Oxygen Vacancies for Enhanced Photocatalytic CO_2 Reduction. *Appl. Catal. B* **2019**, *243*, 566–575. [CrossRef]

43. Kang, M.; Liang, J.; Wang, F.; Chen, X.; Lu, Y.; Zhang, J. Structural Design of Hexagonal/Monoclinic WO_3 Phase Junction for Photocatalytic Degradation. *Mater. Res. Bull.* **2020**, *121*, 110614. [CrossRef]
44. Shi, W.; Guo, X.; Cui, C.; Jiang, K.; Li, Z.; Qu, L.; Wang, J.-C. Controllable Synthesis of Cu_2O Decorated WO_3 Nanosheets with Dominant (001) Facets for Photocatalytic CO_2 Reduction under Visible-Light Irradiation. *Appl. Catal. B* **2019**, *243*, 236–242. [CrossRef]
45. Dong, G.; Huang, X.; Bi, Y. Anchoring Black Phosphorus Quantum Dots on Fe-Doped $W_{18}O_{49}$ Nanowires for Efficient Photocatalytic Nitrogen Fixation. *Angew. Chem. Int. Ed.* **2022**, *61*, e202204271. [CrossRef] [PubMed]
46. Hui, X.; Li, L.; Xia, Q.; Hong, S.; Hao, L.; Robertson, A.W.; Sun, Z. Interface Engineered $Sb_2O_3/W_{18}O_{49}$ Heterostructure for Enhanced Visible-Light-Driven Photocatalytic N_2 Reduction. *Chem. Eng. J.* **2022**, *438*, 135485. [CrossRef]
47. Zou, W.; Shao, Y.; Pu, Y.; Luo, Y.; Sun, J.; Ma, K.; Tang, C.; Gao, F.; Dong, L. Enhanced Visible Light Photocatalytic Hydrogen Evolution via Cubic CeO_2 Hybridized g-C_3N_4 Composite. *Appl. Catal. B* **2017**, *218*, 51–59. [CrossRef]
48. Fang, X.; Chen, L.; Cheng, H.; Bian, X.; Sun, W.; Ding, K.; Xia, X.; Chen, X.; Zhu, J.; Zheng, Y. Homojunction and Ohmic Contact Coexisting Carbon Nitride for Efficient Photocatalytic Hydrogen Evolution. *Nano Res.* **2023**, *16*, 8782–8792. [CrossRef]
49. Yang, J.; Hou, Y.; Sun, J.; Liang, T.; Zhu, T.; Liang, J.; Lu, X.; Yu, Z.; Zhu, H.; Wang, S. Cu Doping and Ti_3C_2OH Quantum Dots Co-Modifications of $Zn_3In_2S_6$ Boosted Photocatalytic Reduction of CO_2 to CO via Accelerating Carriers Transfer and Enhancing CO_2 Adsorption and Activation. *Chem. Eng. J.* **2023**, *452*, 139522. [CrossRef]
50. Wang, K.; Gu, G.; Hu, S.; Zhang, J.; Sun, X.; Wang, F.; Li, P.; Zhao, Y.; Fan, Z.; Zou, X. Molten Salt Assistant Synthesis of Three-Dimensional Cobalt Doped Graphitic Carbon Nitride for Photocatalytic N_2 Fixation: Experiment and DFT Simulation Analysis. *Chem. Eng. J.* **2019**, *368*, 896–904. [CrossRef]
51. Yang, J.; Guo, Y.; Jiang, R.; Qin, F.; Zhang, H.; Lu, W.; Wang, J.; Yu, J.C. High-Efficiency "Working-in-Tandem" Nitrogen Photofixation Achieved by Assembling Plasmonic Gold Nanocrystals on Ultrathin Titania Nanosheets. *J. Am. Chem. Soc.* **2018**, *140*, 8497–8508. [CrossRef] [PubMed]
52. Ren, X.; Xia, M.; Chong, B.; Yan, X.; Lin, B.; Yang, G. Transition Metal Modified 3DOM WO_3 with Activated N≡N Bond Triggering High-Efficiency Nitrogen Photoreduction. *Chem. Eng. Sci.* **2022**, *257*, 117734. [CrossRef]
53. Zhao, Y.; Zhao, Y.; Shi, R.; Wang, B.; Waterhouse, G.I.N.; Wu, L.Z.; Tung, C.H.; Zhang, T. Tuning Oxygen Vacancies in Ultrathin TiO_2 Nanosheets to Boost Photocatalytic Nitrogen Fixation up to 700 nm. *Adv. Mater.* **2019**, *31*, e1806482. [CrossRef] [PubMed]
54. Liu, Y.; Liang, L.; Xiao, C.; Hua, X.; Li, Z.; Pan, B.; Xie, Y. Promoting Photogenerated Holes Utilization in Pore-Rich WO_3 Ultrathin Nanosheets for Efficient Oxygen-Evolving Photoanode. *Adv. Energy Mater.* **2016**, *6*, 1600437. [CrossRef]
55. Wang, J.; Zhang, Q.; Deng, F.; Luo, X.; Dionysiou, D.D. Rapid Toxicity Elimination of Organic Pollutants by the Photocatalysis of Environment-Friendly and Magnetically Recoverable Step-Scheme $SnFe_2O_4/ZnFe_2O_4$ Nano-Heterojunctions. *Chem. Eng. J.* **2020**, *379*, 122264. [CrossRef]
56. Yang, G.; Chen, D.; Ding, H.; Feng, J.; Zhang, J.Z.; Zhu, Y.; Hamid, S.; Bahnemann, D.W. Well-Designed 3D $ZnIn_2S_4$ Nanosheets/TiO_2 Nanobelts as Direct Z-Scheme Photocatalysts for CO_2 Photoreduction into Renewable Hydrocarbon Fuel with High Efficiency. *Appl. Catal. B* **2017**, *219*, 611–618. [CrossRef]
57. Shi, K.; Wang, F.; Li, X.; Huang, W.; Lu, K.; Yu, C.; Yang, K. Defect-engineered WO_{3-x} nanosheets for optimized photocatalytic nitrogen fixation and hydrogen production. *J. Mater. Sci.* **2023**, *58*, 16309–16321. [CrossRef]
58. Yang, Z.; Wang, J.; Wang, J.; Li, M.; Cheng, Q.; Wang, Z.; Wang, X.; Li, J.; Li, Y.; Zhang, G. 2D WO_{3-x} Nanosheet with Rich Oxygen Vacancies for Efficient Visible-Light-Driven Photocatalytic Nitrogen Fixation. *Langmuir* **2022**, *38*, 1178–1187. [CrossRef]
59. Wang, L.; Wang, S.; Cui, D.; Li, M.; Yang, X.; Li, F.; Xu, L. Z-scheme heterojunctions with double vacancies semiconductors MoO_{3-x} and Fe-doped $W_{18}O_{49}$ for photocatalytic nitrogen fixation. *J. Alloys Compd.* **2022**, *927*, 167003. [CrossRef]
60. Huang, H.; Wang, X.-S.; Philo, D.; Ichihara, F.; Song, H.; Li, Y.; Li, D.; Qiu, T.; Wang, S.; Ye, J. Toward visible-light-assisted photocatalytic nitrogen fixation: A titanium metal organic framework with functionalized ligands. *Appl. Catal. B Environ.* **2020**, *267*, 118686. [CrossRef]
61. Xu, H.; Wang, Y.; Dong, X.; Zheng, N.; Ma, H.; Zhang, X. Fabrication of In_2O_3/In_2S_3 microsphere heterostructures for efficient and stable photocatalytic nitrogen fixation. *Appl. Catal. B Environ.* **2019**, *257*, 117932. [CrossRef]
62. Hu, T.; Jiang, G.; Yan, Y.; Lan, S.; Xie, J.; Zhang, Q.; Li, Y. Facile synthesis of Fe single-atom porous photocatalysts via direct metal atomization achieving efficient photocatalytic nitrogen fixation. *J. Mater. Sci. Technol.* **2023**, *167*, 248–257. [CrossRef]
63. Huang, X.; Shi, Y.; Liu, C.; Wang, Z.; Bi, J.; Yu, J.C.; Wu, L. Enhanced photocatalytic nitrogen fixation on Cu_2O clusters/MIL-100(Fe) heterojunction. *Appl. Surf. Sci.* **2023**, *640*, 158443. [CrossRef]
64. Li, Q.; Zhao, Z.; Bai, X.; Tong, X.; Yue, S.; Luo, J.; Yu, X.; Wang, Z.; Wang, Z.; Li, P.; et al. Tunable and stable localized surface plasmon resonance in $SrMoO_4$ for enhanced visible light driven nitrogen reduction. *Chin. J. Catal.* **2021**, *42*, 1763–1771. [CrossRef]
65. Li, C.; Gu, M.; Gao, M.; Liu, K.; Zhao, X.; Cao, N.; Feng, J.; Ren, Y.; Wei, T.; Zhang, M. N-doping TiO_2 hollow microspheres with abundant oxygen vacancies for highly photocatalytic nitrogen fixation. *J. Colloid Interface Sci.* **2022**, *609*, 341–352. [CrossRef]

66. Wang, W.; Zhou, H.; Liu, Y.; Zhang, S.; Zhang, Y.; Wang, G.; Zhang, H.; Zhao, H. Formation of B-N-C Coordination to Stabilize the Exposed Active Nitrogen Atoms in g-C_3N_4 for Dramatically Enhanced Photocatalytic Ammonia Synthesis Performance. *Small* **2020**, *16*, 1906880. [CrossRef] [PubMed]
67. Liang, C.; Niu, H.-Y.; Guo, H.; Niu, C.-G.; Yang, Y.-Y.; Liu, H.-Y.; Tang, W.-W.; Feng, H.-P. Efficient photocatalytic nitrogen fixation to ammonia over bismuth monoxide quantum dots-modified defective ultrathin graphitic carbon nitride. *Chem. Eng. J.* **2021**, *406*, 126868. [CrossRef]